

**NEUTRON SCALAR POLARIZABILITIES:
MODELING THE ^3He ACTIVE TARGET**

By

MATTHEW T. MULLINS

A thesis submitted to the
Department of Physics
Mount Allison University
in partial fulfillment of the requirements for the
Bachelor of Science degree
with Honours in Mathematics and Physics
May, 2019

ABSTRACT

The known values for the scalar polarizabilities of the neutron have a relatively large experimental error compared to that of the proton. Previously these values were found by analyzing the results of Compton scattering with a deuterium target, but this method has many causes for uncertainty. The A2 collaboration at the Institut für Kernphysik at Johannes Gutenberg Universität in Mainz, Germany, plans to measure the neutron polarizabilities in a new way. Now, similar Compton scattering based experiments will be carried out with a new active target filled with high-pressure ^3He gas. This active target will allow previously unmeasured quantities of the reaction to be analyzed, thus reducing the background noise of the data, and therefore lowering the experimental error. But to do this software has to be used to reconstruct the events within the active target. The new active target and the software used to reconstruct it are still in development; in particular, I will be aiding in the development of the software.

ACKNOWLEDGMENTS

I want to thank David Hornidge for giving me the opportunity to have a hands-on experience with such a massive experiment; I think it was great for me to see what working on such a team is like, even if I felt in over my head at times. I believe that this experience has hugely affected my possible career choices in the future, and has also made future encounters less daunting.

I'd also like to thank Philippe Martel for helping me set up my software and guide me through ANT. Phil also showed me how software was developed and worked on as a team, such as how to use GitHub, and how to build data using the terminal, how to work using an SDK, and how to debug software using breaks.

I'd also like to thank user 'Baron,' who was my tutor for coding in c++ and developing software, as I had previously minimal experience with code this complex. He helped me understand much of the basic building blocks of object-oriented coding such as encapsulation, inheritance, polymorphism and abstraction. He also helped me with questions regarding data such as a signed vs. unsigned variable, and how data is parsed in through arrays.

Finally, I'd like to thank the A2 Collaboration as a whole for being so welcoming of our new group, and providing opportunities for us to socialize.

Contents

ABSTRACT	i
ACKNOWLEDGMENTS	ii
TABLE OF CONTENTS	iii
LIST OF FIGURES	iv
LIST OF TABLES	vii
GLOSSARY	ix
1 INTRODUCTION	1
1.1 The Standard Model	1
1.2 Quantum Chromodynamics	3
1.3 Coherent Compton Scattering	4
1.4 Scalar Polarizabilities	5
1.4.1 Electric Polarizability	6
1.4.2 Magnetic Polarizability	7
1.4.3 The Neutron Problem	8
2 EXPERIMENT	10
2.1 Mainz Microtron	10
2.1.1 Racetrack Microtrons	12
2.1.2 Harmonic Double-Sided Microtron	13
2.2 Photon Tagging	13
2.2.1 Bremsstrahlung Production	14
2.2.2 Photon Tagger	15
2.3 Active Helium Target	16
2.3.1 Design	17
2.3.2 Principle of Operation	18
2.4 Detectors	19
2.4.1 Crystal Ball	19

2.4.2	Two-Armed Photon Spectrometer	19
2.5	Background Simulations	20
2.5.1	AcquMC	21
2.5.2	Geant4	21
2.5.3	ANT	21
3	DATA ANALYSIS	23
3.1	ANT Overview	23
3.1.1	Input Commands	23
3.1.2	Data Structure	23
3.2	Unpacker	24
3.2.1	Initializing Elements	24
3.2.2	Data Emplacement	25
3.2.3	Data Emplacement Confirmation	26
3.3	Physics	28
3.3.1	Summing Energies	28
3.3.2	Reconstruction	29
4	DISCUSSION AND OUTLOOK	32
4.1	Summary and Results	32
4.2	Future Work	32
	REFERENCES	34

List of Figures

1.1	The basic table of the standard model, including the newly discovered Higgs boson which was confirmed on July 4 th , 2012 [CER18]. In the table the particles are categorized by colour: purple for quarks, green for leptons, red for Gauge bosons, and yellow for the Higgs boson [Wik18].	2
1.2	Diagram of Compton Scattering. A photon of wavelength λ is absorbed by the target, which in this case is ${}^3\text{He}$, and is re-emitted at angle θ with a wavelength λ' . The vector indicates the direction of the recoiling nucleus.	5
1.3	Second (1.2) and third (1.3) order expansion of the Hamiltonian for Compton scattering.	5
1.4	A depiction of the effect of an electric field upon a composite particle, with the left diagram representing before the field is applied and the right representing while being applied [Hor19a].	6
1.5	A depiction of the effect of a magnetic field upon a composite particle, with the left diagram representing before the field is applied and the right representing while being applied [Hor19a].	7
1.6	A diagram of a proton between the poles of a magnet. The diamagnetic contribution causes the pions to rotate, and the paramagnetic contribution causes the quarks to align in the direction of the south pole [Hor19b].	8
2.1	Floorplan of the MAMI facility located at the Institut für Kernphysik at Johannes Gutenberg Universität in Mainz, Germany. Included here is the A1, A2, A4, and X1 halls, the double sided Microtron (HDSM), and the three racetrack microtrons (RTMs) [Cal08].	11
2.2	A single racetrack microtron (RTM). The line and arrow represent the path and direction of the electrons, the two large rectangular shapes to the left and right are magnets used to bend the electrons, the long rectangle at the bottom is a LINAC, and the boxes above it are the focusing devices that help keep the electrons on track [Cal08].	12

2.3	A depiction of the RTM system we have at MAMI. The beam initially travels through the LINAC and then three RTMs of increasing size. The variables listed correspond to the values at MAMI, with a maximum output of 855 MeV by RTM3 [Cal08, MAM13].	13
2.4	A depiction of the newer more powerful Harmonic Double-Sided Microtron (HDSM), here four magnets are used instead of two. This new design allows for a maximum energy of 1558 MeV [Cal08, MAM13].	14
2.5	A depiction of A2 experimental hall's photon tagger. The electron beam is directed onto the radiator depicted at the bottom left of the figure. The propagated photon beam is depicted as the wavy line, and the various angles which the electron beam take are the curving lines coming off the radiator. The beam dump is present right above where the primary beam is labelled, the primary beam being the path travelled by electrons that emit no photon [Rei06].	16
2.6	The newly designed active helium target with its various measurements listed [Ann14].	18
2.7	A diagram of the two major detectors in the A2 experimental hall. The Two-Armed Photon Spectrometer (TAPS) is the hexagonal plane to the lower left, and the Crystal Ball (CB) is the sphere to the upper right. The photon beam is depicted as coming in from the top right [Rei06].	20
3.1	An example of a command used to run ANT. Here, -o specifies the output location, -i in the input location, -s the setup class, and -p the physics class.	23
3.2	The layout of ANT. Depicting the steps required to go from an input to the desired output. Arrows point the direction data is parsed, and boxes represent the genres of classes. The genres that are relevant to the development of the active target are marked with circles, while the desired input and output are marked with triangles.	24
3.3	A detailed detector header file and a corresponding GetGATChannels method for an active target with six detector channels. Since there are six channels, six vector rows must be defined; and therefore GetGATChannels must return six as well.	25

3.4	The ‘for loop’ in NextEvent which emplaces each event to it’s allocated space. The unsigned constant ‘ch’ is equal to a specific element in t.atI, which corresponds to a channel. If ‘ch’ is greater than the number of allocated elements, we know something has gone wrong.	26
3.5	The .root file’s data before (top) and after (bottom) being parsed through ANT. There are 193643 event entries before and after, proving that no data has been lost.	27
3.6	A Codeblock from the new physics class. An event is parsed into the method ProcessEvent, which gives the total energy picked up by the GAT channels. This energy is then plotted onto the histogram in Figure 3.7.	28
3.7	The summed energies being picked up by the GAT. It’s quite similar in comparison to the plot of the individual detector energies but has some slight variance in shape. Also, we can see that there are now 100000 event entries rather than 193643, which seems right as we were getting around two channels hit per event.	29
3.8	This is a Missing Energy plot of $E_\gamma = 200$ MeV made in 2016 by Morris [Mor16]. It displays the events as categorized by a candidate, and maps out the point on the histogram according to missing energy reading. The candidates are considered background noise that we wish to isolate.	30
3.9	This code block is the pseudocode describing what needs to added to the ProcessEvent method. EsumGAT is still the total GAT energy that was created in Section 3.3.1.	31

List of Tables

1.1	Table of the magnetic and electric polarizability of the proton and neutron [Pat16].	9
3.1	Table of the various interactions that can happen within the active target [Mor16].	29

GLOSSARY

ADC	Analogue to Digital Converter
AHT	Active Helium Target
APT	Active Proton Target
CB	Crystal Ball
ChPT	Chiral Perturbation Theory
DAQ	Data Acquisition
G4	Geant4
GAT	General Active Target
HDSM	Harmonic Double Sided Microtron
LINAC	Linear Accelerator
MAMI	Mainz Microtron
PCB	Printed Circuit Board
PMT	Photomultiplier Tube
PTFE	Polytetrafluoroethylene
RTM	Racetrack Microtron
SiPM	Silicone Photomultiplier
SM	Standard Model
QCD	Quantum Chromodynamics

Chapter 1

INTRODUCTION

1.1 The Standard Model

We start with the Standard Model (SM), which was initially named in the 1970s and describes the elementary interactions of particle physics. Pictured in Figure 1.1, the particles are classified into four sections, which are further separated by two different types: quarks and leptons being the fermion type, and the gauge bosons and the Higgs bosons, which as the names imply are the boson type.

The fermion particles obey the Pauli exclusion principle and are of the smallest scale possible, i.e., they do not have a composite structure. The SM is organized by mass, the first column is the first generation and are the particles with the lowest mass; the second column is the second generation, which is larger in mass than the first generation, and the third column is the third generation, which is the largest in mass. As seen in Figure 1.1, the first generation consists of up (u) and down (d), the second charm (c) and strange (s), and the third top (t) and bottom (b).

Other than this, they are notable for all having a half-integer spin, e.g., $1/2$, $3/2$, etc. For each of the twelve fermions listed, there is a respective antiparticle counterpart with an equal and opposite charge. Additionally, each quark has a property known as colour, this is not to be confused by the colour perceived by your eyes. The colour of a quark can be red, green, or blue, making for a total of 36 different quark classifications [Gri08].

Quarks and anti-quarks bind together to create hadrons, which are the baryons and mesons. Specifically, three quarks combine to create a baryon, while a quark

Standard Model of Elementary Particles

		three generations of matter (fermions)			interactions / force carriers (bosons)	
		I	II	III		
mass		$\approx 2.2 \text{ MeV}/c^2$	$\approx 1.28 \text{ GeV}/c^2$	$\approx 173.1 \text{ GeV}/c^2$	0	$\approx 125.09 \text{ GeV}/c^2$
charge		$\frac{2}{3}$	$\frac{2}{3}$	$\frac{2}{3}$	0	0
spin		$\frac{1}{2}$	$\frac{1}{2}$	$\frac{1}{2}$	1	0
		u up	c charm	t top	g gluon	H higgs
	QUARKS	$\approx 4.7 \text{ MeV}/c^2$	$\approx 96 \text{ MeV}/c^2$	$\approx 4.18 \text{ GeV}/c^2$	0	
		$-\frac{1}{3}$	$-\frac{1}{3}$	$-\frac{1}{3}$	0	
		$\frac{1}{2}$	$\frac{1}{2}$	$\frac{1}{2}$	1	
		d down	s strange	b bottom	γ photon	
	LEPTONS	$\approx 0.511 \text{ MeV}/c^2$	$\approx 105.66 \text{ MeV}/c^2$	$\approx 1.7768 \text{ GeV}/c^2$	$\approx 91.19 \text{ GeV}/c^2$	
		-1	-1	-1	0	
		$\frac{1}{2}$	$\frac{1}{2}$	$\frac{1}{2}$	1	
		e electron	μ muon	τ tau	Z Z boson	
		$< 2.2 \text{ eV}/c^2$	$< 1.7 \text{ MeV}/c^2$	$< 15.5 \text{ MeV}/c^2$	$\approx 80.39 \text{ GeV}/c^2$	
		0	0	0	± 1	
		$\frac{1}{2}$	$\frac{1}{2}$	$\frac{1}{2}$	1	
		ν_e electron neutrino	ν_μ muon neutrino	ν_τ tau neutrino	W W boson	
						SCALAR BOSONS
						GAUGE BOSONS VECTOR BOSONS

Figure 1.1: The basic table of the standard model, including the newly discovered Higgs boson which was confirmed on July 4th, 2012 [CER18]. In the table the particles are categorized by colour: purple for quarks, green for leptons, red for Gauge bosons, and yellow for the Higgs boson [Wik18].

and an anti-quark form a meson. This means that mesons have integer spin while baryons have half-integer spin. The force which causes the quarks to bond in this way is known as the strong nuclear force and is mediated by the gluons. An example of such a composite structure is the neutron, which is in-fact a baryon made up of one up quark and two down quarks.

Unlike quarks, leptons are not subject to strong interaction and instead interact via the weak interaction, gravity, and the electromagnetic force. The first generation consists of the electron (e^-) and electron neutrino (ν_e), the second of the muon (μ) and muon neutrino (ν_μ), and the third of the tau (τ) and tau neutrino (ν_τ) as seen in Figure 1.1.

Gauge bosons dictate the interactions between particles, with each type of interaction being mediated with a separate gauge boson. As stated before gluons are

responsible for the strong nuclear force, which increases in magnitude as the quarks get farther apart. This force keeps quarks in bound states, as a considerable amount of energy is required to pull the quarks to a distance in which it is favourable to create new quarks rather than maintain the coupling. As one might guess this is the most influential force by far [Gri08].

Photons are responsible for the electromagnetic force, and the Z and W bosons are responsible for the weak force between particles, leaving only the weak gravitational force without a known gauge boson. This particle is theorized to exist but is not yet contained within the SM; however, the recent confirmation of gravitational waves may help change that.

Last is the Higgs bosons, the newest addition to the SM. Only just recently discovered in 2012 at CERN's Large Hadron Collider, widely known as the world's largest and most powerful particle accelerator. This boson interacts with what is known as the Higgs field, which mediates how much mass a particle has. This interaction is responsible for the measurement of observable masses of particles that are expected to be massless.

As seen in Figure 1.1, the gluon is represented by a (g), the photon by (γ), the Z boson by (Z), the W boson by (W), and the Higgs boson by (H). In contrast to fermions, the gauge and Higgs bosons all have a spin of just one.

1.2 Quantum Chromodynamics

Quantum Chromodynamics (QCD) is the theory that describes the strong interactions between quarks and the formation of hadrons. The strong force interacts quite differently when quarks are separated by a small distance than when a large distance separates them, and thus the theory has been split into two branches.

When quarks are close together, they exhibit what is known as asymptotic free-

dom, where they will not interact much. In this state where the quarks are asymptotically free, they are modelled by the theory of perturbative QCD (pQCD). Probing quarks in this state requires a large amount of energy, but they have the advantage of being modelled by perturbation theory. Putting it simply: the perturbed case can be found by taking the unperturbed case and building upon it [Gri08].

When quarks are far apart the strong forces are at their strongest, and thus are modelled by the non-perturbative QCD theory (non-pQCD). In this branch of the theory, only low energies are required to probe the behaviour, however as the name implies, perturbation theory no longer applies. The non-pQCD models are less understood than the pQCD model, and the region between these two models is even less understood [Hor19a]. One method of furthering our understanding of the non-pQCD region is to use Compton scattering to measure the polarization of observables and build upon this data.

1.3 Coherent Compton Scattering

The basis of much of this experiment will come from the results of Compton scattering, namely coherent Compton scattering. This is when a photon ‘bounces’ off the nucleus as a whole rather than just off of one of the nucleons quasi-freely. We will be using a target of ${}^3\text{He}$, it’s reaction is shown in Equation 1.1.



The scattered photon labelled as λ' in Figure 1.2, can be used to observe the behaviour of ${}^3\text{He}$ under the effects of the external fields. This behaviour is gone over in more detail in Section 1.4. Not only can the λ' be used for this purpose, but the recoiling ${}^3\text{He}$ nuclei as well. How this is done is explained in Section 2.3.

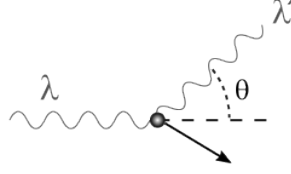


Figure 1.2: Diagram of Compton Scattering. A photon of wavelength λ is absorbed by the target, which in this case is ${}^3\text{He}$, and is re-emitted at angle θ with a wavelength λ' . The vector indicates the direction of the recoiling nucleus.

1.4 Scalar Polarizabilities

The polarizabilities of a composite particle are its fundamental properties, like mass, radius, and charge. In the same way that mass can be said to describe how gravity affects a particle, it can be said that polarizabilities describe how a particle reacts to external EM fields. Here we can look at two different kinds of polarizabilities: scalar and spin.

The scalar polarizabilities are derived from the second-order expansion of the Hamiltonian for the interaction in the incident photon energy shown in Equation 1.2, while the spin polarizabilities are obtained from the third expansion shown in Equation 1.3 [Hor19a].

$$H_{eff}^{(2)} = -4\pi \left[\frac{1}{2} \alpha_{E1} \vec{E}^2 + \frac{1}{2} \beta_{M1} \vec{H}^2 \right] \quad (1.2)$$

$$H_{eff}^{(3)} = -4\pi \left[\frac{1}{2} \gamma_{E1E1} \vec{\sigma} \cdot (\vec{E} \times \dot{\vec{E}}) + \frac{1}{2} \gamma_{M1M1} \vec{\sigma} \cdot (\vec{H} \times \dot{\vec{H}}) \right. \\ \left. - \gamma_{M1E2} E_{ij} \sigma_i H_j + \gamma_{E1M2} H_{ij} \sigma_i E_j \right] \quad (1.3)$$

Figure 1.3: Second (1.2) and third (1.3) order expansion of the Hamiltonian for Compton scattering.

Here α_{E1} and β_{M1} are the electric and magnetic polarizabilities, \vec{E} and \vec{H} are the electric and magnetic field. $\gamma_{E1E1}, \gamma_{M1M1}, \gamma_{E1M1}, \gamma_{M1E1}$ are the various spin polarizabilities, and $\vec{\sigma}$ are the Pauli spin matrices. As a shorthand, we define $E_{ij} = \frac{1}{2}(\nabla_i E_j + \nabla_j E_i)$ and $H_{ij} = \frac{1}{2}(\nabla_i H_j + \nabla_j H_i)$.

The focus of this work will be on scalar polarizabilities rather than the spin; thus we can ignore the third order expansion. Specifically, we are looking at the electric and magnetic scalar polarizability. As said before, the polarizabilities describe how a particle reacts to external electric and magnetic fields. Therefore, determining more accurate values of these two polarizabilities will result in more accurate predictions of how the particles will react in EM fields. As non-pQCD relies on probing quarks with EM fields, more accurate polarizabilities will result in a finer tuned non-pQCD model.

1.4.1 Electric Polarizability

The electric polarizability can be thought of as the ‘stretchability’ of a composite particle. This value corresponds to how easily the particle deforms under an external electric field, and the greater the electric polarizability, the easier it is to deform. This effect is caused by the quarks in the composite particle being attracted to the corresponding direction in the electric field as depicted in Figure 1.4, and thus the particle is ‘stretched’ by this field. Even the neutron, while it exhibits no net electric charge, it is still made up of quarks and thus it too presents this ‘stretching’.

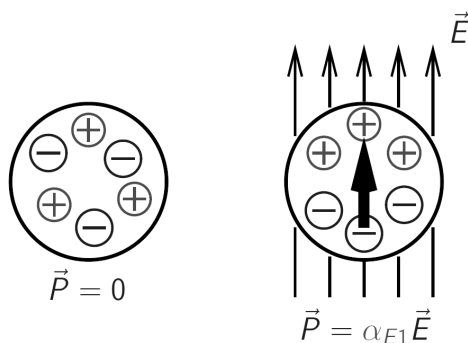


Figure 1.4: A depiction of the effect of an electric field upon a composite particle, with the left diagram representing before the field is applied and the right representing while being applied [Hor19a].

More explicitly, the amount the quarks separate is represented by the equation

$\vec{P} = \alpha_{E1}\vec{E}$, where \vec{P} is the dipole moment. The α_{E1} acts as the proportionality constant between the dipole moment and the electric field, i.e. it's a measurement of how tightly bound the neutron is.

1.4.2 Magnetic Polarizability

Similar to electric polarizability the magnetic polarizability governs how the composite particle reacts to a magnetic field. This can be thought of as the ‘alignability’ of the composite particle. Under the effect of a magnetic field, the quarks that comprise the particle have their magnetic moments rotated to align to the direction of the field as depicted in Figure 1.5.

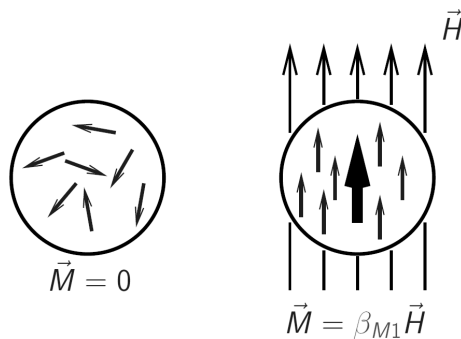


Figure 1.5: A depiction of the effect of a magnetic field upon a composite particle, with the left diagram representing before the field is applied and the right representing while being applied [Hor19a].

Higher magnetic polarizability corresponds to a higher internal alignment of magnetic moments, and thus a larger ‘alignability’. This relation, like the electric polarizability, is linear and expressed through the equation $\vec{M} = \beta_{M1}\vec{H}$, where \vec{M} is the magnetic dipole moment and β_{M1} acts as the proportionality constant between the magnetic dipole moment and the magnetic field.

It turns out for hadrons the magnetic polarizability is a smaller value than electric polarizability. This is because two opposing contributions, known as paramagnetic and diamagnetic contributions, add together create the magnetic polarizability. The

paramagnetic contributions are caused by the internal alignment of the magnetic moments as seen in Figure 1.5, these are the dominant of the two. These contributions attract the magnetic field, while the diamagnetic contributions repel them. The diamagnetic contributions are caused by the induced current by Lenz' Law [Gri17].

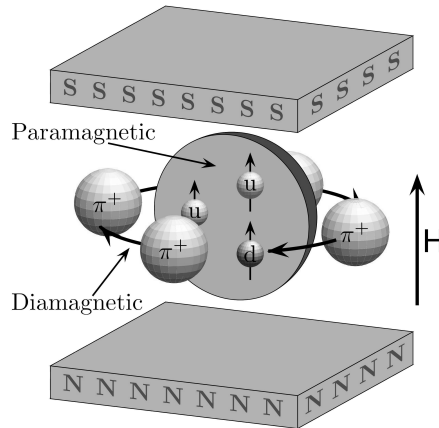


Figure 1.6: A diagram of a proton between the poles of a magnet. The diamagnetic contribution causes the pions to rotate, and the paramagnetic contribution causes the quarks to align in the direction of the south pole [Hor19b].

1.4.3 The Neutron Problem

While the polarizabilities of the proton have been accurately measured, the neutron polarizability errors are larger than desired. As depicted in Table 1.1 the errors of the polarizabilities of the neutron are almost three times than that of the proton! Whereas the polarizabilities for the proton can simply be found through Compton scattering of a free-proton target, it's not as easy for the neutron. This is because the nucleus of the neutron is highly unstable and decays too quickly to be useful. Instead, a more stable nucleus has to be used along with a theoretical model to translate the results to that of the free-neutron target. Previously groups have used the deuteron to take the place of a free-neutron target, but this model introduced too much uncertainty.

Particle	$\alpha_{E1}(10^{-4}\text{fm}^3)$	$\beta_{M1}(10^{-4}\text{fm}^3)$
Neutron	11.8 ± 1.1	3.8 ± 1.2
Proton	11.2 ± 0.4	2.5 ± 0.41

Table 1.1: Table of the magnetic and electric polarizability of the proton and neutron [Pat16].

This new experiment we will not be using the deuteron, and will instead be following a proposed theory called Chiral Perturbation Theory (ChPT) which states that ^3He is more sensitive to the polarizabilities than the deuteron, and can, therefore, be used to model the free-neutron target more accurately [Shu08]. This is because in ^3He the two protons have opposite spin states, effectively cancelling out much of their impact on the experiment. This will cause less dependence on the theoretical model, meaning less sources of uncertainty, and therefore resulting in more accurate measurements of the polarizabilities of the neutron.

Chapter 2

EXPERIMENT

In this chapter, we will describe the various facilities utilized at the A2 experimental hall used to generate and collect the Compton scattering data from a ${}^3\text{He}$ active target. Then an explanation of the various software used to interpret this data will be provided.

2.1 Mainz Microtron

The first part of this experimental setup is an accelerated electron beam. The Mainz Microtron (MAMI), located at the Institut für Kernphysik at Johannes Gutenberg Universität in Mainz, Germany, is the source of the accelerated electron beam for the A2 experimental hall [Kai08] as well as many other collaborations. A graphical representation of this facility can be viewed below in Figure 2.1.

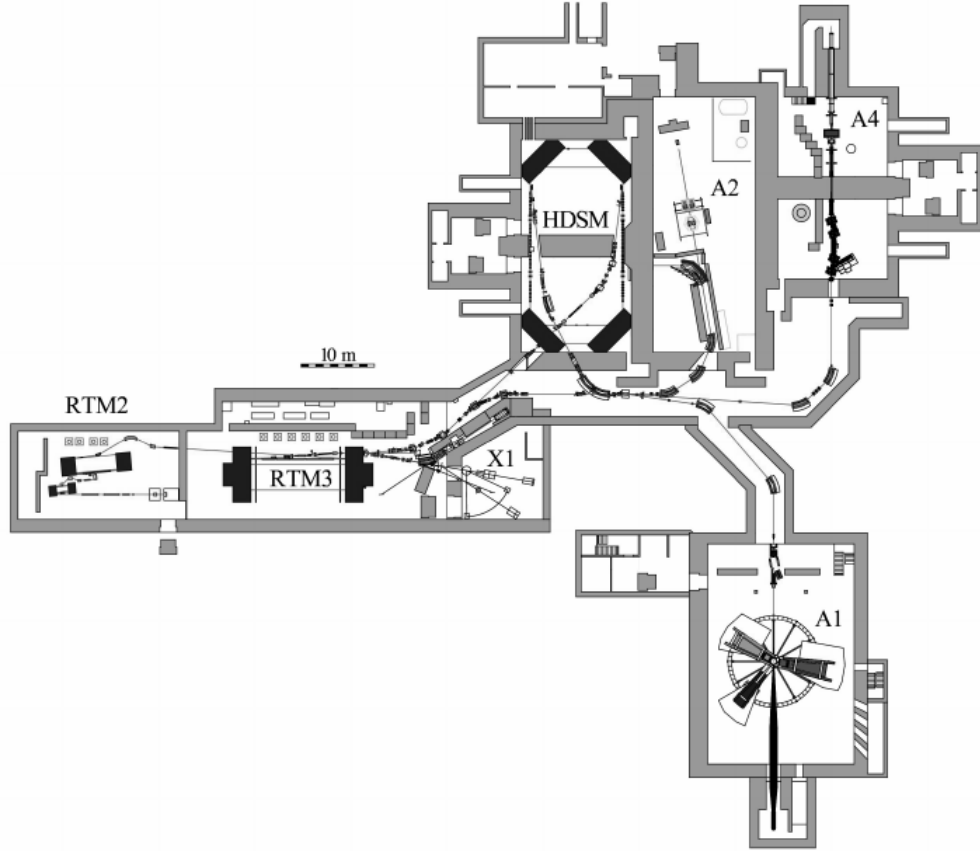


Figure 2.1: Floorplan of the MAMI facility located at the Institut für Kernphysik at Johannes Gutenberg Universität in Mainz, Germany. Included here is the A1, A2, A4, and X1 halls, the double sided Microtron (HDSM), and the three racetrack microtrons (RTMs) [Cal08].

The beam being sent to A2 can only reach a maximum electron energy of 1558 MeV. While this is not very strong compared to other facilities in Europe, it is a continuous-wave beam. This means that the beam is a continuous stream of electrons rather than a beam composed of various densities of particles. Not only that, but the emittance for beam energy is very well defined, with an uncertainty of less than 13 keV [Kai08]. For these reasons, it is ideal for conducting low energy experiments. Before we move on to what we do with this electron beam, we must first explain how the electrons are accelerated to such a level.

2.1.1 Racetrack Microtrons

To accelerate the electrons to the appropriate energy EM fields are used to pull and push the electrons along a set path. The electrons are fed initially through the linear accelerator component (LINAC), which gives them the initial energy necessary for the next apparatus. They are then sent into what's called a racetrack microtron (RTM). In the RTM this path is curved so that the electrons will repeatedly travel through a linear section where they will be accelerated by a linear accelerator. As the electrons gain speed, they have a larger turning radius due to Lorentz force, and thus loops of increasing size have to be made as depicted in Figure 2.2. The magnets must too grow in size to accommodate the path of the electrons. Focusing devices are placed along the track to deter the electron paths from diverging [Cal08].

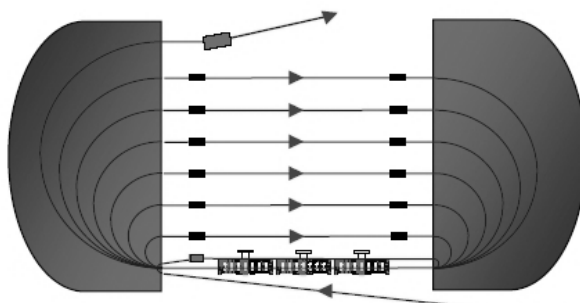


Figure 2.2: A single racetrack microtron (RTM). The line and arrow represent the path and direction of the electrons, the two large rectangular shapes to the left and right are magnets used to bend the electrons, the long rectangle at the bottom is a LINAC, and the boxes above it are the focusing devices that help keep the electrons on track [Cal08].

In this iteration of the racetrack, two magnets bend the electron's path. The electron travels in a straight line before making a 180-degree turn and moving in the opposite direction before making another 180-degree turn [Kai08]. Theoretically we could keep increasing the size of this one RTM to increase the maximum energy of the electrons, but instead, it is much more cost and space efficient to instead build multiple racetracks that feed into each other. Such a system is depicted in Figure 2.3.

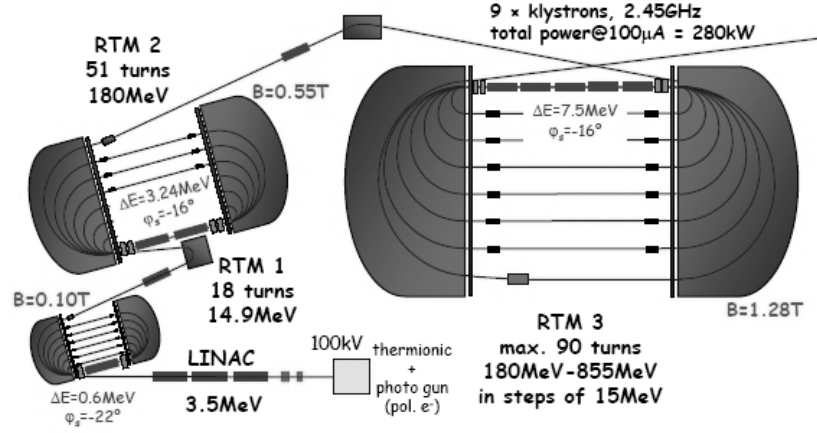


Figure 2.3: A depiction of the RTM system we have at MAMI. The beam initially travels through the LINAC and then three RTMs of increasing size. The variables listed correspond to the values at MAMI, with a maximum output of 855 MeV by RTM3 [Cal08, MAM13].

2.1.2 Harmonic Double-Sided Microtron

When the needed energy surpasses that supplied by RTM3, it is not feasible to create a fourth RTM as it would just be much too large, so instead, an entirely new type of microtron was built. This new microtron has four magnets instead of two and is called the Harmonic Double-Sided Microtron (HDSM) depicted in Figure 2.4. This causes the electrons only to have to take 90 degree turns, which takes less force per magnet to keep them on course, meaning the magnets result in being much smaller in size.

The downside is that the beam is less focused and needs more corrected in the vertical axis of the shaft. For this experiment, we only require an electron energy of 855, so the HDSM is not needed.

2.2 Photon Tagging

With the appropriate photon energies being sent to the A2 experimental hall, it is now time for this beam to be converted to a photon beam. The energies of these

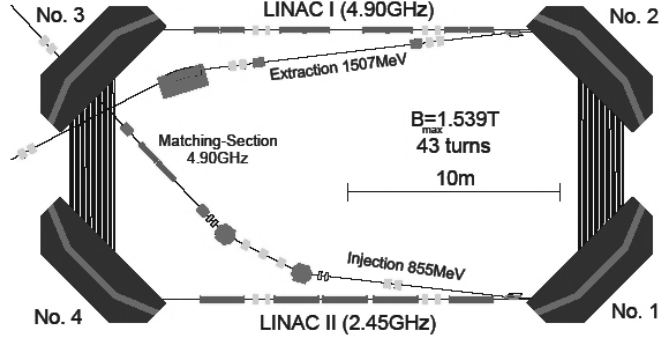


Figure 2.4: A depiction of the newer more powerful Harmonic Double-Sided Microtron (HDSM), here four magnets are used instead of two. This new design allows for a maximum energy of 1558 MeV [Cal08, MAM13].

photons can then be measured using the photon tagger, shown in Figure 2.5.

2.2.1 Bremsstrahlung Production

This conversion is done by sending the electron beam through a radiator with a thin layer of material in it; in this case, a $10 \mu\text{m}$ thick slice of copper was used.

While the electron is passing near the positively charged nuclei of the Cu foil, it is deflected by electromagnetic interaction, causing a sudden change in the momentum of the electron. The electron then has a chance of radiating a photon to offset this change and conserve the energy of the reaction; this photon travels in the initial direction of the electron. This is known as bremsstrahlung production, which in German means ‘braking radiation’. This process is represented in the following equation:

$$E_{e^-} = E'_{e^-} + E_{\gamma} \quad (2.1)$$

Where E_{e^-} is the electron energy before bremsstrahlung production, E'_{e^-} is the electron energy after production, and E_{γ} is the energy of the photon. The Cu nuclei are very heavy, causing the recoil energy of the nuclei to be so small that it is negligible, and is therefore excluded from Equation 2.1. This emitted photon then proceeds

farther into the target.

2.2.2 Photon Tagger

The purpose of the photon tagger is to find the energy of the photons being produced from the radiator. We do this not by measuring the photons, but instead the electrons as we know the initial electron energies coming from the beam and can thus use equation 2.1 to find the photon energy without even interacting with the photons.

To do this, we curve the electrons out of the beam using a huge and powerful dipole magnet, as the photons, of course, have no charge they are not affected. The amount the electron is curved by the magnetic field depends on its energy, i.e. those with higher energies are curved less while those with lower energies curve more. The vast majority of electrons in the beam will not produce any photons, and will thus curve at the same angle. Therefore to ignore these electrons they are directed into what is known as a beam dump where they will not be measured. Those that do produce photons will curve into the main detector which has 353 individual scintillators that overlap in such a way that when an electron hits, two neighbouring scintillators will be triggered [McG08]. This is done to reduce the risk of accidentally picking up unwanted noise from outside the experiment. This entire device is shown in detail in Figure 2.5.

When the scintillator registers an electron ‘hit’ it is then able to deduce the radius at which the electron has curved and thus the energy of the electron after photon production which can be used to calculate photon energy as in Equation 2.1.

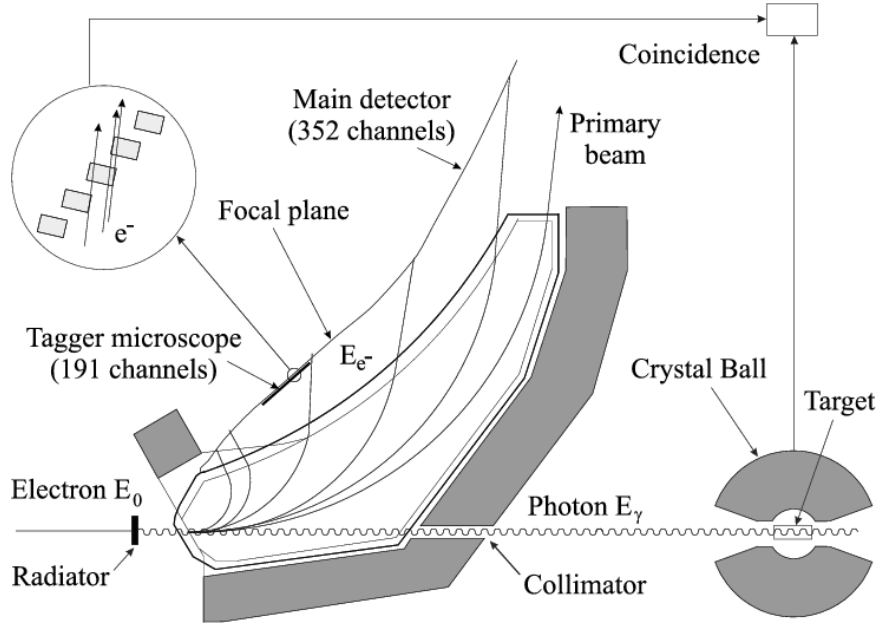


Figure 2.5: A depiction of A2 experimental hall’s photon tagger. The electron beam is directed onto the radiator depicted at the bottom left of the figure. The propagated photon beam is depicted as the wavy line, and the various angles which the electron beam take are the curving lines coming off the radiator. The beam dump is present right above where the primary beam is labelled, the primary beam being the path travelled by electrons that emit no photon [Rei06].

These photon energy values are then compared to the ones found with the detectors discussed in Section 2.4. The distance between where the taggers and detectors measure their data is very well known, so it’s possible to use a timing coincidence to match the values accurately.

2.3 Active Helium Target

The target of a Compton scattering experiment is the object that the photons are going to hit and be emitted from, which in this case is ^3He . This target is built to be active as well, and will, therefore, be called the active helium target (AHT).

The old AHT was a repurposed target used in similar experiments conducted in the MAX-lab in Lund, Sweden. There was a multitude of problems with this design, the

biggest being the need for optical windows to use the photomultiplier tubes (PMT), and the size of the target was too large to fit in the CB when the PMTs are attached. This was an issue since the target needed to be able to contain ^3He at high pressure, and at the required pressure, the windows were liable to break [Ann14]. There is a new design however has been made explicitly for this experiment and fits comfortably within the CB. The sensors are planned to be located inside the target, eliminating the need for optical windows.

2.3.1 Design

While this newest iteration of the active target has not been entirely built, its construction has been well thought out. A prototype has been built, but flaws in the design are still being worked out. The specifications of the design are listed in the following paragraphs.

The target will be built out of aluminum alloy and will be 5 mm thick throughout the outer sides of the structure. The new target is quite long compared to the previous, being a cylindrical shape 800 mm in length and 152 mm at its tallest point. However, without the need for PMTs, the total size is much smaller. A full diagram is shown in Figure 2.6.

The centre cylinder of length 400 mm and inner diameter 102 mm houses the helium, whereas the two protruding tubes of length 200 mm and inner diameter 20 mm are used to separate the windows made of beryllium found at either end of the AHT. These tubes help prevent outside light from making its way into our target. The centre cylinder is lined with two layers, the first being the printed circuit board (PCB) of 1 mm thickness, and the second being 0.5 mm thick polytetrafluoroethylene (PTFE) lining which is layered on top of the PCB and acts as a reflector. Inside the centre cylinder, there are also two aluminized mylar windows, which allow for the

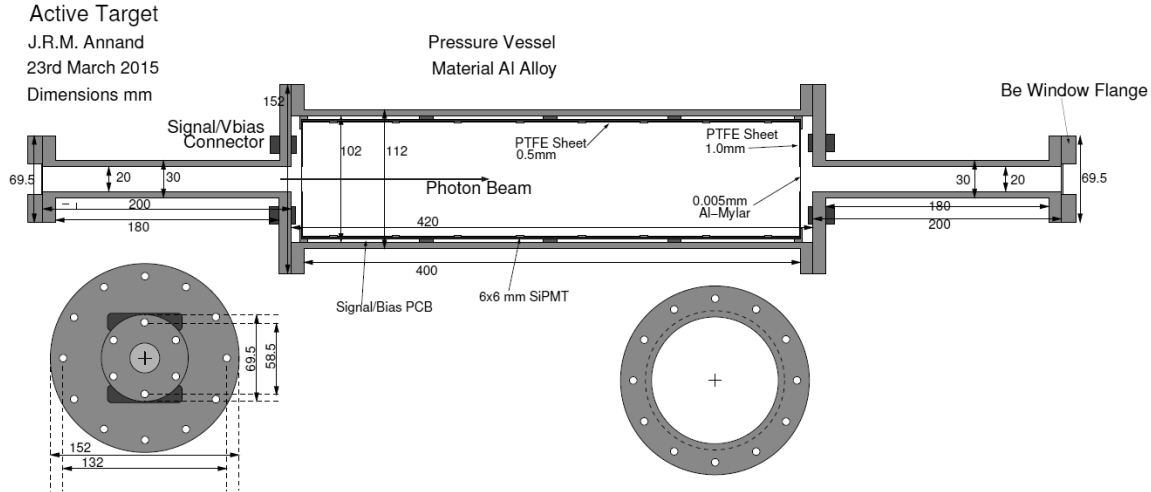


Figure 2.6: The newly designed active helium target with its various measurements listed [Ann14].

photon beam to enter and exit the target. On top of the PCB layer, there are many 6×6 mm squares of silicon photomultiplier (SiPM) cells that will act as our channels for the active target. The helium will be kept at a pressure of 2 MPa to keep the density and rate of Compton scattering high [Ann14]. Nitrogen gas will also be present at a concentration of 1000 ppm. This is because the nitrogen gas boosts the scintillation light to a level readable to the SiPM cells.

2.3.2 Principle of Operation

With an active target, we have two different ways of receiving data from a Compton scattering event, while in a regular target we only have one. A target is set up such that in the event of Compton scattering the scattered photon can be picked up by one of the two main detectors discussed in Section 2.4, but the recoiling helium nucleus is too heavy to go far enough to reach these detectors [MAM13]. Instead, the kinetic energy of the nucleus is transferred to the surrounding nuclei, causing them to excite and emit photons in random directions. The emitted photons will first be in the UV spectrum but will be projected into the visible spectrum as they are absorbed and

then emitted by the nitrogen. These visible flashes of light are then picked up by the SiPMs and be sent to the data acquisition (DAQ) system out in the A2 experimental hall.

2.4 Detectors

As mentioned in the previous section there are two main detectors in the A2 experimental hall surrounding the active target, the Crystal Ball (CB) and the Two-Armed Photon Spectrometer (TAPS). Working together these two detectors cover 96% of the 4π steradians surrounding the target [Unv13].

2.4.1 Crystal Ball

The CB is composed of 672 thallium-doped sodium iodide (NaI(Th)) scintillation crystals arranged as a hollow sphere with an inner radius of 25.3 cm. Each crystal is fitted with a PMT, and an analogue to digital converter (ADC) used to send the appropriate voltage pulses picked up to the DAQ. The target is to be placed in the centre of the CB such that the target is encapsulated by it while undergoing the Compton scattering event. There are gaps in the CB to allow for the passing of the photon beam into it and out of it; however, the CB still covers 93% of the 4π steradians surrounding the target. With the number of sensors, this allows for photons to be measured at a polar angular resolution of 2-3 degrees [Wat05]. The CB can be seen as the spherical object on the right in Figure 2.7.

2.4.2 Two-Armed Photon Spectrometer

The TAPS is placed at the back side of the CB, such that it's hit by any photon beam that exits the hole on that end. It is a wall of 72 lead tungstate (PbWO_4) crystals surrounded by 366 barium fluoride (BaF_2) crystals organized in the shape

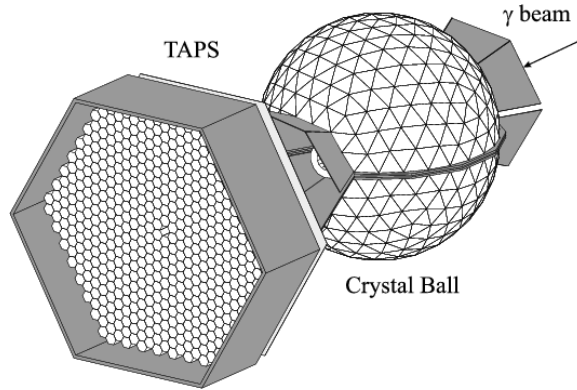


Figure 2.7: A diagram of the two major detectors in the A2 experimental hall. The Two-Armed Photon Spectrometer (TAPS) is the hexagonal plane to the lower left, and the Crystal Ball (CB) is the sphere to the upper right. The photon beam is depicted as coming in from the top right [Rei06].

of a hexagon. While it may be quite large, it is also quite far away from the target, causing it to only cover the remaining 3% of the 4π steradians detector system.

As the photons pass through the target many of them will not generate Compton scattering and will instead travel in a straight line; thus the photon flux at the centre of the TAPS is very high. This is the reason the PbWO_4 crystals are required at the centre of the TAPS, as they are smaller in area than the BaF_2 crystals. Through the use of plastic veto tiles, the TAPS is also able to detect whether a particle is neutral or charged. The TAPS can be seen as the hexagonal plane on the left in Figure 2.7.

2.5 Background Simulations

Before this experiment may take place, we must first run simulations to see if it's possible. This experiment has never been conducted before with this type of target, and thus correctly simulating the results is critical. In this case, simulating results requires many software applications to be run in tandem. The process order is AcqMC into Geant, into ANT. With the results given by ANT we will be provided with the data required to interpolate our data found in the real experiment.

2.5.1 AcquMC

The first of the software, written in C++ by Dr. J.R.M. Annand, is called AcquMC. It generates the initial events of the simulation using Monte Carlo methods [Ann14]. The program must be adequately supplied with the right variables such as the number of events, beam energy, reaction type, and the target element itself. It then generates the reaction kinematics of this experiment and outputs this data in a ROOT ntuple, ROOT being the modular scientific toolkit created by CERN [CER19b].

2.5.2 Geant4

The second piece of software, developed as a toolkit by CERN, is called Geant4 (G4). The information from AcquMC is fed into Geant4 and organized as histograms, similar in format to that received when conducting an actual experiment. It does this by a complicated geometric tracking procedure of the particles and how they interact with the EM field to find where they would be detected by the detector and what would their appropriate energies be. Our code, in particular, was primarily developed by previous students [Hoo17, Abe16]. The output G4 is formatted as a ROOT tree file, which will be parsed into ANT [CER19a].

2.5.3 ANT

The third piece of software, developed in house at A2, is called ANT. ANT takes in data, real or simulated, and reconstructs the events within the target. By doing this, we can identify the particles present in the reaction and organize them into histograms, such as one depicting missing energies. These generated histograms prove to be very useful, as they can be cross-referenced with experimental results. In this case, it will aid in finding the polarizabilities of the neutron. In previous years AcquRoot was used for this purpose, but now the A2 collaboration has opted to

switch to ANT. The development ANT for the active target and the screening out undesirable background data is the focus of the work in this thesis [A219].

Chapter 3

DATA ANALYSIS

3.1 ANT Overview

In this chapter, I will provide a brief overview of ANT, precisely the areas in which I have worked on. I will then go over what I have done and why it is required.

3.1.1 Input Commands

To start ANT the user must run a command in the terminal and select a variety of options corresponding to what reaction and what results they'd like to reconstruct. As an example, the command I used to develop my missing energy plot is depicted in Figure 3.1.

```
Ant -i /home/.../PPN_out.root -p GAT_MissingEnergy -s Setup_2016_06_Active -o output_mc.root
```

Figure 3.1: An example of a command used to run ANT. Here, `-o` specifies the output location, `-i` in the input location, `-s` the setup class, and `-p` the physics class.

3.1.2 Data Structure

In Figure 3.2 we see ANT's data structure, with `AqcuRaw` and `A2Geant` meaning real and simulated data. The data are then brought through the unpacker class, the `SlowControlManager`, a specified physics class which utilizes the `reconstruct` class, and is then outputted as `.root` file histogram. The `SlowControlManager` doesn't need to be edited so it can be ignored. There is also the previously mentioned setup class which is specific to each experiment. This class gives ANT some values it needs to know about the experiment, such as the beam energy.

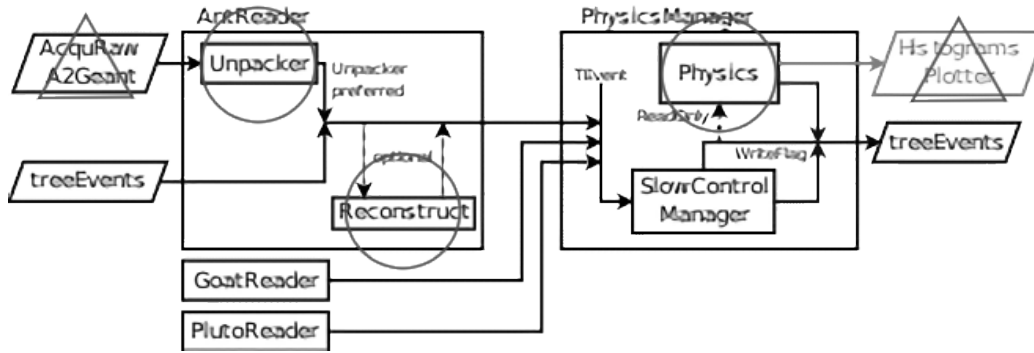


Figure 3.2: The layout of ANT. Depicting the steps required to go from an input to the desired output. Arrows point the direction data is parsed, and boxes represent the genres of classes. The genres that are relevant to the development of the active target are marked with circles, while the desired input and output are marked with triangles.

3.2 Unpacker

3.2.1 Initializing Elements

Before the data are unpacked, we must first initialize a range of elements for this data to be stored, one element for each channel. This is done through a detector class, specific to which detector the data belongs to. Since the active target is a new type of detector a new detector class, which I have opted to call the General Active Target (GAT) class, must be added. The code that I've developed is heavily based off of the Active Proton Target (APT) detector class, written by Abernethy [Abe16].

My goal was to take this code and have it applicable to a more general case, as the code that Abernethy had written only worked an active target that had six channels. To do this, the method `GetGATChannels` was implemented. This method returns the number of channels as specified in the setup class, as seen in Figure 3.3. To call this method, the setup of each active target must be included in the GAT detector file. As a formalization of this change to a more general case, every instance of the acronym APT in ANT was changed to GAT.

After `InitElements` initialize the elements, `buildMappings` is then called. This

```
//defines and sets a vector to be used for GAT.h and subsequently GAT.cc
//number of rows must be equal to GAT_channels defined in setup
const std::vector<ant::exconfig::detector::GAT::Element_t>
ant::exconfig::detector::GAT_2017::elements_init =
{
    // channel, ADC #, TDC #
    { 0, 200, 300},
    { 1, 201, 301},
    { 2, 202, 302},
    { 3, 203, 303},
    { 4, 204, 304},
    { 5, 205, 305}
};

// defines number of channels, will be specific to each active target
unsigned int Setup_2016_06_Active::GetGATChannels()
{
    return 6;
}
```

Figure 3.3: A detailed detector header file and a corresponding GetGATChannels method for an active target with six detector channels. Since there are six channels, six vector rows must be defined; and therefore GetGATChannels must return six as well.

method maps out the time and magnitude of the events as they are fed into ANT.

3.2.2 Data Emplacement

After this space has been initialized, it's the unpacker class's job to take the inputted real or raw data and temporarily place it to this allocated space. It does this with the method NextEvent, which is triggered for every event inputted into ANT. After the event is reconstructed and graphed on the histogram via the physics class, the initialized space is then cleared for the next event's data to take its place. It does this through a series of 'for loops' which emplaces the data for each of the detectors.

The definition of emplacing is to assign a position to an object, and in c++ this corresponds to appending a new element to the end of a container. In this case, it merely means placing the energy and time of the data at the end of a temporary array called 'hits.'

Since the GAT is a new detector, it also needed a 'for loop' in this method and was thus created. It will throw an error if it finds that any of the inputted events fall

outside the range of the initialized channels, so say if data with 64 active channels is inputted and GetGATChannels gives only six channels, an error will be thrown back.

```

// fill GAT Hits
// loops for each row
for(int i=0;i<int(t.atI().size());i++) {

    // Change depending on how the active target feeds in GetNChannel
    const unsigned ch = (t.atI[i]);

    // activated if channel # is outside of the channel range
    if(ch >= GAT_detector->GetNChannels())
        throw Exception("GAT channel number out of bounds " + to_string(ch) + " / " + to_string(GAT_detector->GetNChannels()));

    const Detector_t::Type_t det = Detector_t::Type_t::GAT;
    hits.emplace_back(
        LogicalChannel_t{det, Channel_t::Type_t::Integral, ch},
        TDetectorReadHit::Value_t{GeVtoMeV*t.atE[i]}
    );
    hits.emplace_back(
        LogicalChannel_t{det, Channel_t::Type_t::Timing, ch},
        TDetectorReadHit::Value_t{t.atI[i]}
    );
}

```

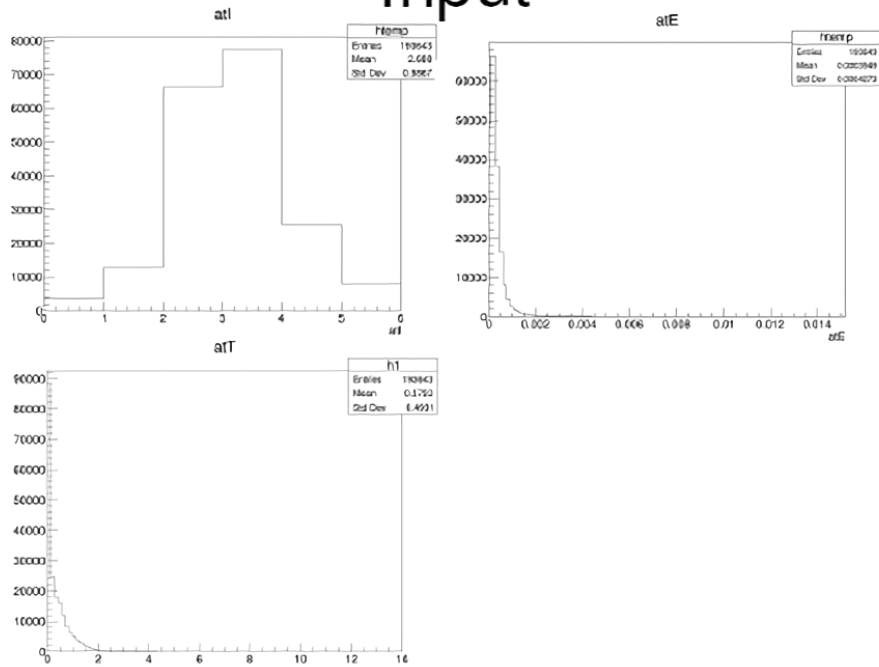
Figure 3.4: The ‘for loop’ in NextEvent which emplaces each event to it’s allocated space. The unsigned constant ‘ch’ is equal to a specific element in t.atI, which corresponds to a channel. If ‘ch’ is greater than the number of allocated elements, we know something has gone wrong.

3.2.3 Data Emplacement Confirmation

Data issues are a common problem with software engineering, thus to prove that none of this data is being lost, a physics class was created. This physics class simply took data that was being emplaced and plotted it without altering it. These histograms also had the same x and y range and the same number of bins as the inputted .root file. This was to show that the data was successfully parsed through without the loss or alteration of data.

As shown in Figure 3.5, the data have been properly emplaced through ANT. This can be observed as the general trends of the plots are the same before and after. Looking closer, we can see that the entries count is the same before and after, showing that not a single event was lost in this process!

Input



Output

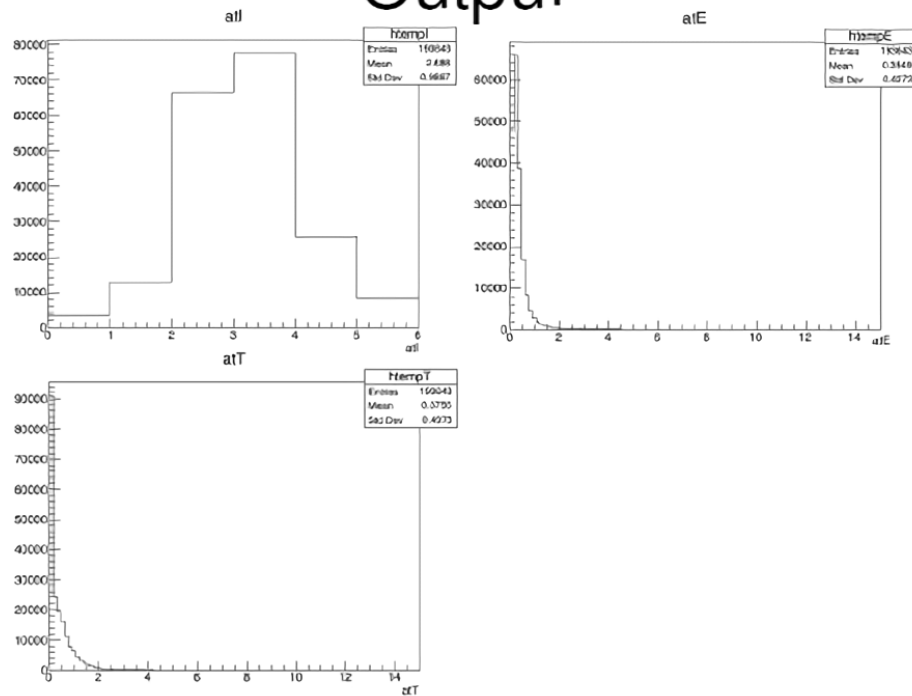


Figure 3.5: The .root file's data before (top) and after (bottom) being parsed through ANT. There are 193643 event entries before and after, proving that no data has been lost.

3.3 Physics

3.3.1 Summing Energies

After checking that everything is working correctly, we want to start reconstructing the events within the target. But first, we must sum the detected energies for each event. This is because, as mentioned in Section 2.3.2, the kinetic energy of the ^3He nucleus is transferred to the surrounding nuclei, meaning that the energy from an event scatters and is often picked up by multiple detectors.

```
// process for a SINGLE event
void GAT_SummedEnergy::ProcessEvent(const TEvent& event, manager_t&)
{
    double EsumGAT = 0; // GAT Energy Sum
    for(auto& hit : event.Reconstructed().DetectorReadHits)
    {
        // screens out data we don't need
        if(hit.DetectorType == Detector_t::Type_t::GAT && hit.ChannelType == Channel_t::Type_t::Integral)
        {
            EsumGAT += hit.Values[0].Calibrated;
        }
    }
    // fills histogram
    TotalEnergy->Fill(EsumGAT);
    t.Tree->Fill();
}
```

Figure 3.6: A Codeblock from the new physics class. An event is parsed into the method ProcessEvent, which gives the total energy picked up by the GAT channels. This energy is then plotted onto the histogram in Figure 3.7.

As events are passed into this physics class they go through the method ProcessEvent, which performs operations on them before filling histogram(s). As the detected channels go through the ‘for loop’ pictured in Figure 3.7, data corresponding to variables we don’t care about is screened out by the ‘if statement’, such as CB channels readings. A temporary double, EsumGAT, was introduced and is equal to the energy picked up by the active target during an event. It is then this double, that’s passed into the histogram and plotted.

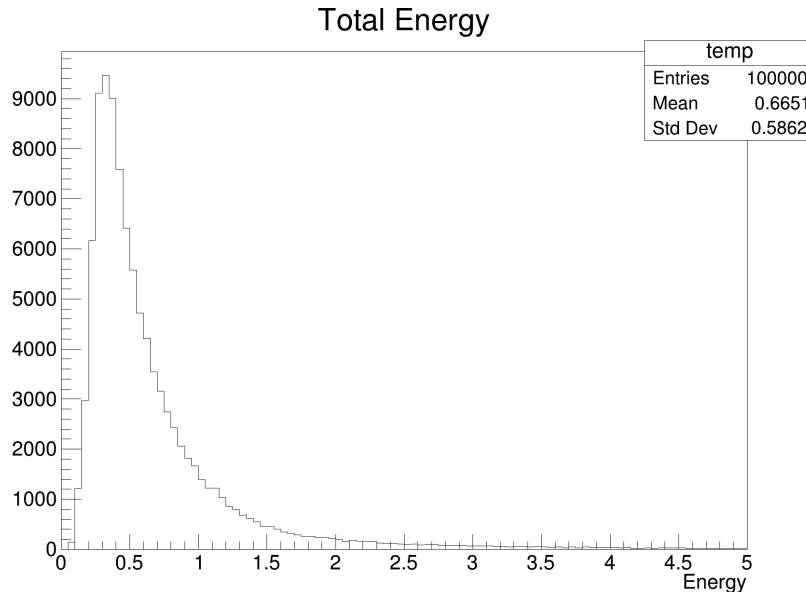


Figure 3.7: The summed energies being picked up by the GAT. It’s quite similar in comparison to the plot of the individual detector energies but has some slight variance in shape. Also, we can see that there are now 100000 event entries rather than 193643, which seems right as we were getting around two channels hit per event.

3.3.2 Reconstruction

With this summed energy we now want to reconstruct the events into candidates. These candidates represent the different reactions that can occur besides coherent Compton scattering as described in Equation 1.1. They are neutral pion production, quasi-free Compton scattering from the proton, quasi-free neutral pion production from the proton, quasi-free neutral pion production from the deuteron, and pure breakup; their interactions are listed in Table 3.3.2.

Candidate	Interaction
Neutral Pion Production	$\gamma + {}^3\text{He} \rightarrow \pi^0 + {}^3\text{He}$
Quasi-Free Compton Scattering from the Proton	$\gamma + {}^3\text{He} \rightarrow \gamma + p + {}^2\text{H}$
Quasi-Free Neutral Pion Production from the Proton	$\gamma + {}^3\text{He} \rightarrow \pi^0 + p + {}^2\text{H}$
Quasi-Free Neutral Pion Production from the Deuteron	$\gamma + {}^3\text{He} \rightarrow p + \pi^0 + {}^2\text{H}$
Pure Breakup	$\gamma + {}^3\text{He} \rightarrow p + p + n$

Table 3.1: Table of the various interactions that can happen within the active target [Mor16].

Once their candidates are found, they can be graphed and appropriately screened out as one desires as depicted in Figure 3.8.

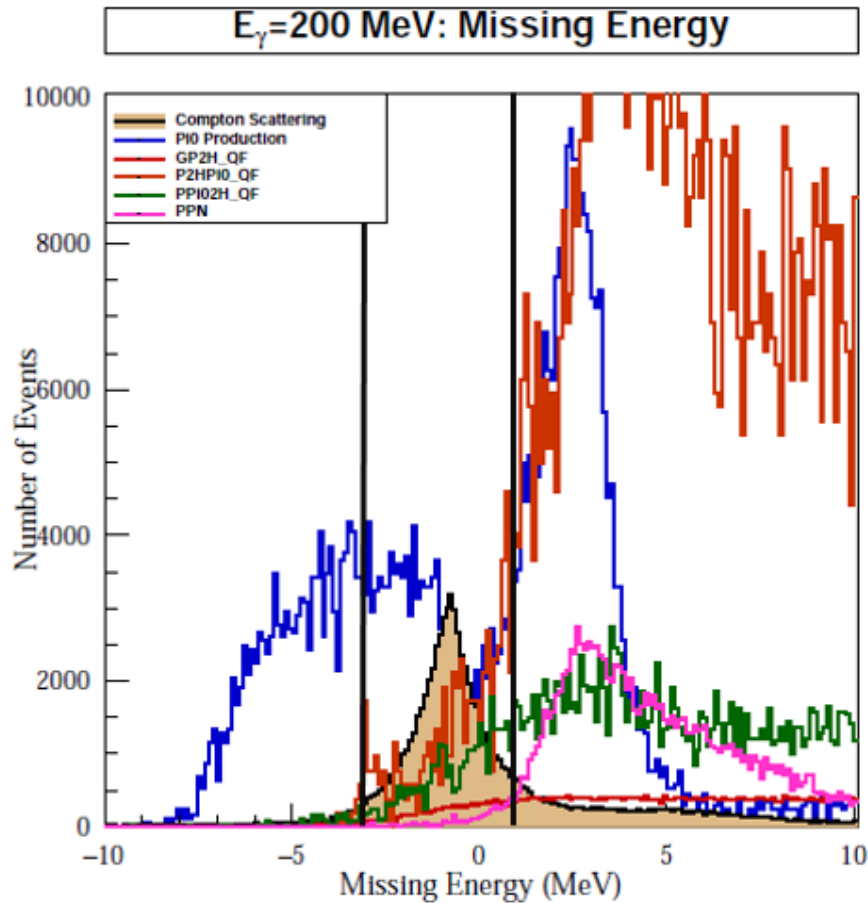


Figure 3.8: This is a Missing Energy plot of $E_\gamma = 200$ MeV made in 2016 by Morris [Mor16]. It displays the events as categorized by a candidate, and maps out the point on the histogram according to missing energy reading. The candidates are considered background noise that we wish to isolate.

Unfortunately, this process involves coding beyond what I can achieve, and I was unsuccessful in developing this part of the software. Instead, I will explain what needs to be done using pseudocode.

```

void GAT_MissingEnergy::ProcessEvent(const TEvent& event, manager_t&)
{
    double EsumGAT = 0; // GAT Energy Sum
    for(auto& hit : event.Reconstructed().DetectorReadHits)
    {
        if(hit.DetectorType == Detector_t::Type_t::GAT && hit.ChannelType == Channel_t::Type_t::Integral)
        {
            EsumGAT += hit.Values[0].Calibrated;
        }
    }

    // add various candidates:
    // Neutral Pion Production
    // Quasi-Free Compton Scattering from the Proton
    // Quasi-Free Neutral Pion Production from the Proton
    // Quasi-Free Neutral Pion Production from the Deuteron
    // Pure Breakup

    // parse data into reconstructor to find which candidates occurred

    // convert photon tagger energy, recolling photon energy, and GAT Energy Sum to find missing energy
    // E_y - E_y' - EsumGAT = E_miss

    // fill histogram with E_miss, catagorized by production type
}

```

Figure 3.9: This code block is the pseudocode describing what needs to be added to the ProcessEvent method. EsumGAT is still the total GAT energy that was created in Section 3.3.1.

First, we construct the various candidates that we will use to categorize the reactions. Then, the event will be parsed into the reconstructor class mentioned in Section 3.1.2. The reconstructor class will categorize the hits within the event as one of the various candidates. Then, the missing energy will be found using the equation $E_{\text{miss}} = E_{\gamma} - E_{\gamma'} - E_{\text{sumGAT}}$, where E_{γ} and $E_{\gamma'}$ is the photon energy before and after, and E_{sumGAT} is the summed energy calculated in Section 3.3.1. This missing energy will then be filled into a histogram, categorized by a candidate. In the end, the results should be similar to the missing energy plot in Figure 3.8.

Chapter 4

DISCUSSION AND OUTLOOK

4.1 Summary and Results

I was able to code the unpacker section of ANT for the GAT and proved that the data were being properly parsed through the system. I then constructed a physics class to sum the energies of the channels to find the energy of the recoiling ^3He nuclei. We can tell that the graph in Figure 3.7 is correct as it has the same number of entries as the input file has events. However, I was unable to reconstruct the data into candidates, as the code was too advanced for me. If this were to be done, we would hopefully plot a histogram similar to the one in Figure 3.8 but with less background noise.

4.2 Future Work

This is a very large experiment that has been worked on for years, and there is still much to do. The most obvious thing that needs to be worked on is the physics class for reconstructing events using the active target. After that, the biggest thing holding us back is that the new active target is not finished, limiting us only to use simulated data. As advanced as AcquMC and Geant4 are there are limits to what they simulate, such as timing coincidence mentioned in Section 2.2.2. ANT has to be coded to be able to match the incoming data accordingly with the readings picked up by the photon tagger, but as we don't have these values, we can't even develop the code. As of now, the top priority should be finishing the active target and taking a couple of runs with it in the A2 Collaboration beam hall to collect data. Hopefully,

this upcoming summer Michael Perry's work will finish up the active target, and we will be able to move forward with the development of the software.

References

- [A219] A2, Ant, <https://github.com/A2-Collaboration/ant>, 2019.
- [Abe16] S. Abernathy, various code, 2016, ANT Analysis Toolkit, Institut für Kernphysik at Johannes Gutenberg Universität.
- [Ann14] J. R. M. Annand and B. Strandberg, Mainz Microtron MAMI: Proposal for an Experiment - Compton Scattering on the He Isotopes with an Active Target, 2014.
- [Cal08] S. Caliori, *Measurement of the Neutron Electric Form Factor at $Q^2 = 1.58(\text{GeV}/c)^2$* , Ph. D. Thesis, Università Degli Studi Di Trento, 2008.
- [CER18] CERN, The higgs boson, 2018.
- [CER19a] CERN, Geant4, <https://geant4.web.cern.ch>, 2019.
- [CER19b] CERN, Root, <https://root.cern.ch>, 2019.
- [Gri08] D. Griffiths, *Introduction to Elementary Particles*, WILEY-VCH, Second Edition, 2008.
- [Gri17] D. Griffiths, *Introduction to Electrodynamics*, Cambridge University Press, Fourth Edition, 2017.
- [Hoo17] K. Hood, *Proton Detection Efficiency with the Active Polarized Target*, Honours Thesis, Mount Allison University, 2017.
- [Hor19a] D. Hornidge, Compton Scattering and Polarizabilities, 2019.
- [Hor19b] D. Hornidge, private communication, 2019.
- [Kai08] H. Kaiser, K., *Nuclear Instruments and Methods in Physics Research Section A*, volume 593, 2008.
- [MAM13] MAMI, Compton Scattering on the He Isotopes With an Active Target, Technical report, 2013, Institut für Kernphysik at Johannes Gutenberg Universität.
- [McG08] J. McGeorge, J. Kellie, and J. Annand, *The European Physical Journal A: Upgrade of the Glasgow Photon Tagging Spectrometer for Mainz MAMI-C*, volume 37, 2008.
- [Mor16] M. Morris, *Neutron Scalar Polarizabilities: Background Simulations for Experimental Extraction via Compton Scattering from ^3He* , Honours Thesis, Mount Allison University, 2016.

- [Pat16] C. Patrignani, Particle Physics Booklet **40**, 89 (2016).
- [Rei06] A. Reiter, The European Physical Journal **30**, 461 (2006).
- [Shu08] D. Shukla, A. Nogga, and D. Phillips, Analyzing the Effects of Neutron Polarizabilities in Elastic Compton Scattering off ^3He , 2008.
- [Unv13] M. Unverzagt, *The European Physical Journal A: Quasi-free photoproduction of η -mesons off ^3He nuclei*, volume 49, 2013.
- [Wat05] D. Watts, Crystal Ball at MAMI Daniel Watts, Univ. of Edinburgh (UK) For the Collaboration, 2005.
- [Wik18] Wikipedia, Standard model, 2018.